Manuscript prepared for Atmos. Meas. Tech.
with version 5.0 of the LaTeX class copernicus.cls.
Date: 5 May 2014

A New Differential Absorption Lidar to Measure Sub-hourly Fluctuation of Tropospheric Ozone Profiles in the Baltimore - Washington D.C. Region

J. T. Sullivan[1,2], **T. J. McGee**[3], **G. K. Sumnicht**[4], **L. W. Twigg** [4], **and R. M. Hoff** [1,2]

[1]Department of Atmospheric Physics, University of Maryland Baltimore County (UMBC), Baltimore, MD, United States
[2]Joint Center for Earth Technologies (JCET), Baltimore, MD, United States
[3]Code 614.0, NASA Goddard Space Flight Center, Greenbelt, MD, United States
[4]Science Systems and Applications Inc., Lanham, MD, United States

Correspondence to: John T. Sullivan
(johnsullivan@umbc.edu)

A New Differential Absorption Lidar to Measure Sub-hourly Fluctuation of Tropospheric Ozone Profiles in the Baltimore - Washington D.C. Region

Abstract. Tropospheric ozone profiles have been retrieved from the new ground based National Aeronautics and Space Administration (NASA) Goddard Space Flight Center TROPospheric OZone DIfferential Absorption Lidar (GSFC TROPOZ DIAL) in Greenbelt, MD (38.99°N, 76.84°W, 57 meters ASL) from 400 m to 12 km AGL. Current atmospheric satellite instruments cannot peer through the optically thick stratospheric ozone layer to remotely sense boundary layer tropospheric ozone. In order to monitor this lower ozone more effectively, the Tropospheric Ozone Lidar Network (TOLNet) has been developed, which currently consists of five stations across the US. The GSFC TROPOZ DIAL is based on the Differential Absorption Lidar (DIAL) technique, which currently detects two wavelengths, 289 and 299 nm. Ozone is absorbed more strongly at 289 nm than at 299 nm. The DIAL technique exploits this difference between the returned backscatter signals to obtain the ozone number density as a function of altitude. The transmitted wavelengths are generated by focusing the output of a quadrupled Nd:YAG laser beam (266 nm) into a pair of Raman cells, filled with high pressure hydrogen and deuterium. Stimulated Raman Scattering (SRS) within the focus generates a significant fraction of the pump energy at the first Stokes shift. With the knowledge of the ozone absorption coefficient at these two wavelengths, the range resolved number density can be derived. An interesting atmospheric case study involving the Stratospheric-Tropospheric Exchange (STE) of ozone is shown to emphasize the regional importance of this instrument as well as assessing the validation and calibration of data. The retrieval yields an uncertainty of 16-19% from 0-1.5 km, 10 - 18% from 1.5 -3 km, and 11 - 25% from 3 km to 12 km. There are currently surface ozone measurements hourly and ozonesonde launches occasionally, but this system will be the first to make routine tropospheric ozone profile measurements in the Baltimore-Washington D.C. area.

1 Introduction

Tropospheric ozone above the ground level has been historically difficult to measure directly due to its relatively short lifetime and nonlinear formation (Stevenson et al. (2013)). It is an important greenhouse gas, pollutant, and source of OH radicals. Its contribution to global warming from the preindustrial era to the present is regarded as the third most important, following those of carbon dioxide (CO_2) and methane (CH_4) (IPCC (2007)). Ozone is also toxic to humans and vegetation because it begins oxidizing biological tissue and causes harmful respiratory effects in instances of long exposure (McDonnell et al. (1999)). Tropospheric ozone within the Planetary Boundary Layer (PBL) in the Baltimore-Washington D.C. area is typically dominated by photochemistry with local ozone precursor emissions, but within the free troposphere there are other source classifications such as 1) Stratospheric-Tropospheric Exchange (STE), 2) advection from upwind sources and 3) regional redistri-

bution from convection and/or lightning (Thompson et al. (2008)).

During an STE event, large concentrations of ozone are exchanged between the stratosphere and the troposphere during certain meteorological events, such as an unusually low Polar or Subtropical jet stream (Langford (1999)). A recent analysis of summertime tropospheric ozone profiles in the Baltimore-Washington D.C. area showed that STE accounted for greater than 50% of the free tropospheric ozone column on 17% of days sampled (Yorks et al. (2009)). The second source of ozone in the free troposphere occurs when ozone is transported aloft or advected with varying layer thickness and concentration downwind of the major ozone precursor production sites, potentially resulting in an ozone exceedance for rural and less populated areas (NCADAC (2013)). The subsidence of the ozone layer aloft has been shown to cause air quality issues for a region that may not have actually produced the ozone or its precursors (Langford et al. (2010)). The third source of ozone in the free troposphere is not a primary source but rather the ozone precursor NO_X is induced by lightning flashes, which accounts for 5 - 10% of the overall tropospheric ozone budget (Schumann and Huntrieser (2007),Yuan et al. (2012)).

With such dynamic sources of ozone in the troposphere, it is essential to monitor the vertical distribution of tropospheric ozone. Although the vertical location of atmospheric trace gases (such as CO_2) are remotely monitored by satellites, these measurements in the ultra-violet (UV) regime, especially near the surface, are difficult to obtain due to the optically thick stratospheric ozone layer strongly attenuating the signal (Fishman et al. (1990)). Ozone profiles from the Tropospheric Emission Spectrometer (TES) and the Ozone Mapping Instrument (OMI) have been reported, but have usually required a large amount of prior knowledge and/or ancillary satellites (such as NASA's Microwave Limb Sounder (MLS)) are needed to determine the residual amount of ozone in the troposphere (Ziemke et al. (2006), Bowman et al. (2002)). Even if the tropospheric ozone profile is reported, it may be a seasonal or monthly mean, in which the variability of ozone gives the profiles marginal statistical value (Thompson et al. (2003)). For ozone profiles that are reported for a direct overpass, due to the large footprint of the satellite, this method may not be able to resolve small scale fluctuations of tropospheric ozone concentration, especially during quickly evolving pollution episodes. By monitoring and analyzing tropospheric ozone from a ground based instrument, such as an ozone lidar, the signal is not attenuated via stratospheric ozone and the tropospheric ozone concentrations can be detected at a much higher temporal and vertical resolution.

For these reasons, the National Aeronautics and Space Administration (NASA) Goddard Space Flight Center TROPospheric OZone DIfferential Absorption Lidar (GSFC TROPOZ DIAL) has been developed to take routine measurements of tropospheric ozone near the Baltimore - Washington D.C. area (Greenbelt, MD 38.99°N, 76.84°W, 57 meters ASL). This instrument has been developed as part of the ground-based Tropospheric Ozone Lidar NETwork (TOLNet), which currently consists of five stations across the United States (http://www-air.larc.nasa.gov/missions/TOLNet/). The primary purpose of the instruments within TOLNet is to provide regular, high fidelity profile measurements of ozone within the troposphere, particularly the changing ozone dynamics and laminae inside the PBL. The network will also serve to validate the upcoming GEOstationary Coastal and Air Pollution Events (GEO-CAPE) mission, scheduled to be launched in the 2020 timeframe. Another objective of TOLNet is to identify a brassboard ozone lidar instrument that would be suitable to populate a network to address the needs of NASA, the Environmental Protection Agency (EPA), and the National Oceanic and Atmospheric Administration (NOAA) air-quality scientists and managers who increasingly express a desire for ozone profiles.

Similar ground based instruments have been developed in TOLNet (McDermid et al. (2002), Alvarez et al. (2011), Kuang et al. (2013)), but the GSFC TROPOZ DIAL is the first to measure ozone profiles in the Mid-Atlantic region. Aside from the site at the Jet Propulsion Laboratory's Table Mountain Facility (JPL TMF), this is the only instrument currently utilizing high-pressure Stimulated Raman Scattering (SRS) cells for wavelength generation (Haner and McDermid (1990)). Because the remote JPL TMF site is in the Angeles National Forest at an altitude of 2.3 km ASL, the GSFC TROPOZ DIAL will be the first system to use this technique to determine quantitative ozone profiles near sea level directly in an urban environment.

At the surface, in situ UV analyzers and photometers are the most common form of ozone monitors. These instruments utilize photometry and the known extinction coefficient at a specific UV wavelength (usually 254 nm with a Mercury vapor lamp) and the Beer-Lambert Law to derive the known ozone concentration in a volume of sampled gas. The reduction in light intensity between the two photodetectors over a known sampled path length is directly related to the ozone concentration. Most monitors require calibration with a zero air source and are usually accurate to within 5% of the known value (Puzak (1987)) and can report values with very high temporal resolution.

The EPA has set up a network of surface ozone monitoring and detection that covers a large spatial and temporal region in the last few decades (Demerjian (2000)). These ozone concentrations are typically reported in hourly average values or 8 hour average values and are useful for analyzing surface trends in ozone. As mentioned earlier ozone can be transported aloft and advected, preventing the surface monitors from truly representing the ozone distribution in that region. The vertical distribution of ozone is an important parameter in analyzing daily and seasonal trends and events that surface monitors cannot provide. If there is a dramatic change

in ozone at the surface that cannot be explained with the in situ data, it is essential to analyze the vertical profile of ozone above the surface as a function of time..

The common historical method for vertical ozone detection is sending a balloon-borne electrochemical concentration cell (ECC) instrument through the atmosphere, but this may not be on the continuous scale that is necessary to fully characterize small scale fluctuations in ozone. The ECC profiles ozone with a 100 m vertical resolution from the surface to 35-km altitude with an accuracy of 10% for tropospheric mixing ratios, except in the case of very low mixing ratios (<10 ppb) when the accuracy may be degraded to 15% (Newchurch et al. (2003), Komhyr et al. (1995), Oltmans et al. (1996)).

Due to complex formation and transport of ozone it is typically necessary to measure for extended periods of time to fully characterize an ozone pollution episode, which favors a continuous measurement as opposed to an isolated or several profiles. Using lidar techniques in mostly cloud free conditions, it is possible to measure the continuous vertical distribution of the dynamic atmosphere by detecting the return signal as a function of altitude. A stationary, continuous time series of vertical profile measurements can be obtained more cost effectively with a DIAL instrument such as described in this paper than with the launch of multiple ozonesondes.

There have been successful DIAL instruments that have utilized the ground based monitoring method, dating back to the 1970's, with a focus on water vapor (Browell et al. (1979)) and temperature profiles (Murray et al. (1980)). These concepts were then successfully modified and demonstrated to yield accurate results for ozone detection (Uchino et al. (1978), Megie et al. (1985), Browell (1989)), with specific emphasis on monitoring and maintaing a historic record of ozone trends in the stratosphere (McDermid et al. (1991), McGee et al. (1993), McGee et al. (1995)). Because tropospheric ozone can create air pollution episodes, it was necessary to develop DIAL instruments, such as the GSFC TROPOZ DIAL, and a network, such as TOLNet, to make routine measurements of the ozone concentrations in the lower free troposphere and the PBL, which can fluctuate much more rapidly that that of the stratospheric ozone.

Similar instruments have been deployed as nadir viewing airborne systems in previous NASA (Browell et al. (1983), Browell et al. (1987), Browell et al. (1993)) and NOAA (Senff et al. (2010)) missions. Although there have been successful measurements of tropospheric ozone profiles using these instruments, there is a sizable operational cost increase and logistical preparation for aircraft systems over ground based instruments (Ancellet and Ravetta (1998)). Although an airborne experiment has many advantages, especially with the use of onboard in situ monitors and remote sensing instruments, it can be difficult to quantify ozone near the surface due to aviation restrictions. Furthermore, past efforts to predict and monitor high levels of ozone in large cities (Houston (Banta et al. (2005)) and Los Angeles (Menzies and Shumate (1978)) from airborne missions have been hampered by the lack of information of the ozone profile and the extent of vertical mixing in the first few kilometers above the surface (Morris et al. (2010)).

The metropolitan area surrounding the GSFC TROPOZ DIAL is affected by locally produced pollutants from highly populated urban areas as well as ozone precursors advected from the Ohio River Valley/Appalachian mountain regions. Depending on the meteorological conditions, these pollutants can cause non-localized unfavorable air quality issues for smaller rural areas as well as the Chesapeake Bay watershed to the south and east. If the eastward propagation of pollutants is inhibited, a stagnant air mass over the Baltimore-Washington D.C. area results, and is the ideal condition for a high pollution episode (Delgado et al. (2014)). During these forecasted high ozone episodes, the GSFC TROPOZ DIAL has been designed to move from routine monitoring to continuous monitoring. The Mid-Atlantic region displays a moderate amount of seasonal ozone variability with the highest concentrations occurring in the late July time period (Lehman et al. (2004)). Because of this, during the fall and winter seasons, the TROPOZ focuses its observations on monitoring ozone in the free troposphere and the aforementioned source contributions, such as STE. This paper investigates the steps necessary to construct the GSFC TROPOZ DIAL in order to retrieve and better characterize the vertical distribution of tropospheric ozone in the Baltimore-Washington D.C. area, in which a regionally important validation test case of an unusually low tropopause, resulting in the exchange of high amounts of ozone between the stratosphere and the lower free troposphere, or STE, is presented and analyzed.

2 The Differential Absorption Lidar (DIAL) Method

Fundamentally, the DIAL method relies on the fact that the ozone molecule has a strongly varying spectral absorption curve in ozone's Hartley band region. Figure 1, adapted from Malicet et al. (1995), illustrates the ozone absorption cross section (σ_{O_3}) and the TROPOZ DIAL wavelengths that were chosen for the large gradient in ozone absorption $(\Delta\sigma_{O_3})$, which will yield usable atmospheric information. Different colors in the figure correspond to the temperature dependence of the absorption cross sections. This method is optimized when the ratio of the difference in the ozone absorption cross section to the difference in wavelength $(\Delta\sigma_{O_3}/\Delta\lambda)$ is maximized within certain atmospheric constraints.

Retrieval of useful ozone profiles during daytime hours requires that the instrument utilizes wavelengths less than 300 nm to avoid saturation of the detectors from sunlight, and to maximize the signal to noise ratio (SNR) of the system (Proffitt and Langford (1997)). Although the ozone absorption curve continues to rise sharply as the wavelength de-

creases (increasing the $\Delta\sigma_{O_3}/\Delta\lambda$), the signal is attenuated much too strongly to yield usable information above above the PBL. Essentially, shorter wavelengths are absorbed so strongly by ozone that the return signal would be unusable above the PBL, especially during pollution episodes. These issues constrain the choice of wavelengths to between 280 and 300 nm. This ensures the system has a large enough signal to easily retrieve ozone profiles through the PBL and into the lower free troposphere.

From Figure 1, 288.9 nm has an absorption cross section nearly 3 times as large as 299.1 nm and both wavelengths can be generated reliably (and much more cost-effectively than dye or tunable cavity lasers) using SRS in high pressure Raman cells (Haner and McDermid (1990)). The transmitted wavelengths are generated by focusing the output of two frequency-quadrupled Neodymium-doped Yttrium Aluminum Garnet (Nd:YAG) laser beams (266 nm), each into a pair of high pressure Raman cells, one filled with hydrogen and the other deuterium. SRS within the focus generates a significant fraction of the pump energy at the first Stokes shift. With the knowledge of the ozone absorption coefficient at these two wavelengths, the range resolved ozone number density can then be derived. The more absorbing wavelength, at 288.9 nm, is called the "on" wavelength and the less absorbing wavelength, at 299.1 nm, is called the "off" wavelength. This process of SRS and the generation of the necessary DIAL wavelengths will be discussed more in the Experimental Construction section of the paper. Because the inelastic Raman conversion is done prior to transmission into the atmosphere, and detection of atmospheric scattering is done at these same transmitted wavelengths, the TROPOZ retrieval used is an elastic technique.

2.1 Introduction to Elastic Lidar

The general lidar equation, taken from Middleton and Spilhaus (1953), is for elastic backscatter in a homogeneous volume of the atmosphere. The elastic lidar equation is,

$$P(r) = P(0)\eta\frac{A}{(r^2)}\frac{c\tau}{2}\beta(r)e^{[-2\int_0^r \alpha(r')dr']} + P_b, \quad (1)$$

where $P(r)$ is the power received from range r, $P(0)$ is the average transmitted power during the laser pulse at the surface, η is the receiver efficiency, A is the receiver area, r is the range to the scattering volume, c is the speed of light, τ is the laser pulse duration, β and α are, respectively, the atmospheric backscatter coefficient and atmospheric extinction coefficient at range r, and P_b is the background radiation at the transmitted wavelength.

Writing equation (1) for P_{on} (the lower and more absorbed wavelength) and P_{off} (the higher and less absorbed wavelength) and taking their ratio, many of the system constants drop out. Assuming the solar background can be quantified and subtracted, this can be rewritten as

$$\frac{P_{on}(r)}{P_{off}(r)} = \frac{\beta_{on}(r)}{\beta_{off}(r)}e^{[-2\int_0^r(\alpha_{on}(r)-\alpha_{off}(r))dr]}. \quad (2)$$

Assuming ozone has negligible scattering, the extinction coefficient can be regarded as the absorption coefficient. The absorption coefficients, assuming that the sampled volumes have the same number density of ozone, can be written as,

$$\alpha_{on}(r) - \alpha_{off}(r) = N_{o_3}\Delta\sigma_{O_3} - \Delta\alpha_{atmosphere}, \quad (3)$$

where N_{O3} is the ozone number density and $\Delta\sigma_{O_3}$ is the difference in corresponding ozone absorption cross sections taken for the two wavelengths in Figure 1. The term, $\Delta\alpha_{atmosphere}$, is the difference in the scattering properties of the atmosphere between the two DIAL wavelengths. This includes spectral differences in Rayleigh scattering, aerosols, and other interfering gases that have similar absorption properties in the "on" and "off" wavelengths.

Finally the DIAL equation can be written in terms of the ozone number density as,

$$N_{o_3}(r) = \frac{1}{2\Delta\sigma_{O_3}}\frac{d}{dr}ln[\frac{P_{on}(r)}{P_{off}(r)}\frac{\beta_{off}(r)}{\beta_{on}(r)}] + \frac{\Delta\alpha_{atmosphere}}{\Delta\sigma_{O3}}. \quad (4)$$

In reality, lidar return signals are not recorded or analyzed as continuous functions, but rather as values in discrete range bins, Δr. It is then possible to write the discrete DIAL equation (Milton and Woods (1987)) in terms of the range bins specified, other interfering gases (IG) and aerosol corrections as,

$$N_{o_3} = \frac{1}{2\Delta\sigma_{O_3}\Delta r}\ln(\frac{P_{off}(r+\Delta r)}{P_{off}(r)}, \frac{P_{on}(r)}{P_{on}(r+\Delta r)} - C) - D \quad (5)$$

where,

$$C = \frac{\beta_{off}(r+\Delta r)}{\beta_{off}(r)}\frac{\beta_{on}(r)}{\beta_{on}(r+\Delta r)} \quad (6)$$

and

$$D = \frac{\Delta\alpha_{mol}}{\Delta\sigma_{O_3}} + \frac{\Delta\alpha_{aer}}{\Delta\sigma_{O_3}} + \frac{N_{IG}\Delta\alpha_{IG}}{\Delta\sigma_{O_3}}. \quad (7)$$

Equation (5) is referred to as the DIAL equation and it is of great interest because it is a self calibrating technique that can determine the number density of ozone with only the known ozone absorption cross sections and the power returned to each detector.

The correction term C is due to the derivative in the amount of photons backscattered to the detector from the

ambient atmosphere. This can be a combination of Rayleigh scattering and aerosol scattering if aerosols are present. Rayleigh extinction (which is the first term in D) is typically based on a λ^{-4} scaling, which develops a slight difference in the molecular extinction that is fairly easy to interpolate (Measures (1983)) with additional meteorological terms for corrections given by a reference standard atmosphere (U.S. Standard (1976)). With the knowledge of the Rayleigh extinction values, the Rayleigh backscatter term in C is computed using the assumed Rayleigh phase function.

The second term in D is due to the presence of aerosols and the wavelength dependence of the aerosol extinction coefficient. Depending on the optical properties of the aerosols in the atmosphere during the measurement, this value can change as well, leading to an additional necessary correction (Bösenberg (1998)). In most cases the correction for the additional backscattered light from aerosol gradients to the detector is much larger than the necessary correction for the aerosol extinction correction at these wavelengths (Weitkamp (2006)). The aerosol correction term in D is determined using an iterative method, in which using various valid assumptions it is possible to determine the necessary ozone number density correction. The correction is then coupled with an assumed lidar ratio to determine the correction factor due to aerosols in C. This will be discussed further in the Data Processing section of this paper.

The third term in D is due to the interference of external interfering gases (IG), such as sulfur dioxide (SO_2) and nitric oxide (NO_2). In the wavelength region used for the present work, (SO_2) has relatively similar absorption cross sections to ozone, but the number density, $(N_{IG}) = (N_{SO_2})$, is typically so low that the contribution it makes to the calculation of D is small compared to that from the Rayleigh or aerosol terms. Nitric oxide (NO_2) has similar extinction cross sections which increase with respect to wavelength, but for the current DIAL wavelengths, the result should be reasonably unaffected (Kovalev and Eichinger (2004)).

3 Experimental Construction

3.1 Raman Cells and Stimulated Raman Scattering (SRS)

Although previous work has shown accurate tropospheric ozone retrievals with dye laser sources (Kuang et al. (2011)), and with Ce:LiCAF in a tunable cavity (Senff et al. (2010)), they are expensive and typically delicate systems. The lasers are also required to undergo frequent maintenance procedures and rigorous optimizations during normal operation of the crystals and cavities due to small temperature fluctuations. For these reasons it was advantageous to move toward the use of a stable Nd:YAG laser with the known fourth harmonic frequency pumping a pair of high-pressure Raman cells to generate the transmitted frequencies.

SRS is a direct two-photon, third-order nonlinear optical process, which results in inelastic light scattering without the requirement of phase matching (Mollenauer et al. (1992)). This process is efficient for gases such as hydrogen and deuterium because they have high-frequency vibrational modes and narrow spectral linewidths (Shen and Bloembergen (1965)). Multiple orders of Stokes frequencies are subsequently generated, but for use in this experiment, only the first Stokes shift in each Raman gain medium is useful.

In order to maximize the generation of the first Stokes frequency, a low numerical aperture pumping geometry and a long optical interaction length (Carlsten et al. (1984)) has been established which is the reason for the length of the Raman cells (76 cm) and the focal points (f = 1 m) of the lenses. Because this process is a photon to photon conversion method it is also favorable to have the largest volume available to increase efficiency of the SRS (Falsini et al. (1985)). A low-angle pumping geometry can also reduce the angle condition that is auspicious for phase matched four wave mixing (Duncan et al. (1986)).

This difference in frequency emitted and pumped is directly related to the energy difference between the first excited state and the ground state in the Raman active gas, which is known as the Raman frequency and is adapted from Measures (1983) in Table 1. Therefore, the Raman frequency of the Raman active gas is independent of the absolute energy of the pump photon and the energy of the generated photon is a function of the pump frequency and the species used as the Raman active gas. In the steady state, this process yields the continuous generation of coherent light pulses with the same phase as the pump photons.

The steady-state gain coefficient for the vibrational stimulated Raman scattering is related to the photon conversion efficiency in the system and can be written as

$$\gamma = \frac{2N_j{\lambda_s}^3}{\pi hc\Gamma}\frac{d\sigma}{d\omega}, \tag{8}$$

where λ_s is the first Stokes wavelength, N_j is the Boltzmann number density, Γ is the Raman full line width, $\frac{d\sigma}{d\omega}$ is the differential Raman scattering cross section, h is Planck's constant, and c is the speed of light (Komine (1986)).

For this to be an efficient technique, the steady-state gain must be at an appropriate threshold level to induce the first order Stokes frequencies, while suppressing higher order frequencies. A straightforward method to increase the number density, N_j, is to increase the pressure of the gas in the confined Raman cell volume. Although this does increase the steady state gain, it has an adverse effect on the overall conversion efficiency for the first Stokes shift because the gain grows so large that it begins to activate other higher order processes, collision effects, motional narrowing and four wave matching (Witkowicz and May (1976), Dion and May (1973)).

One other important factor is that the Raman full line width, Γ, is linearly dependent on the total pressure of the cell in the pressure region of interest (Murray and Javan (1972)). Because of this, the steady state gain and photon conversion efficiency are more efficient at higher pressures due to the broadening Raman full line width.

Therefore, to obtain the benefits of the high-pressure regime, while minimizing the effects of an unnecessarily high Raman active number density, a buffer gas has been added to the Raman active gas. Helium has been used, as it is not a Raman active medium in the wavelength regime of ozone detection.

3.2 Raman Cell Characterization

There is a discussion of this method of using a Nd:YAG laser and Raman cells to produce appropriate wavelengths for ozone detection in Haner and McDermid (1990), which was the starting point for the empirical Raman tests that were performed to optimize each Raman cell. Because of the sensitivity of the photon conversion efficiency in laser beam characteristics, such as pump beam diameter and confocal beam parameter entering each Raman cell, it was necessary to test the cells for various pressures and buffer gas concentrations. Unlike other instruments described in the literature, this instrument is housed inside a portable trailer, which has limited the optical interaction length of the Raman cells to 1.8 m. Due to these constraints, the Raman cells were completely designed and fabricated internally for the specific application for use in the GSFC TROPOZ DIAL.

The simplest way to analyze the photon efficiency was to adapt a dispersive pellin broca prism to separate the wavelengths into discrete spots and subsequently view the beam with a fluorescent card. This provided the ability to qualitatively determine which pressure combinations suppressed higher order Stokes shifts and which magnified higher orders. Power measurements of the beams produced by the various Stokes shifts then allowed a quantitative selection of the optimal partial pressures for each of the Raman active gases. Because this is a direct two-photon conversion process from the pump to the respective first Stokes, it was necessary to obtain a baseline for photon conversion by measuring the power of the pump photons, at 266 nm, passing through an evacuated cell.

The empirical results for hydrogen and deuterium are shown in Figure 2a and Figure 2b. These plots are shown as photon conversion efficiency (left y-axis), residual pump transmission (right y-axis) and the total cell pressure (x-axis). Due to safety concerns regarding the design of the Raman cells, the maximum pressure tested was 1000 psig. Multiple power measurements were taken and each data point corresponds to the mean with uncertainty bars of one standard deviation. Initially, power measurements were made without a buffer gas, but the photon conversion efficiencies were so low (10% or less) that they are not reported in this figure. Once the buffer gas was introduced into the Raman cell, the efficiencies began to improve. The three colors in Figure 2a and 2b correspond to three different pressure combinations in each cell. The line style corresponds to the wavelength of interest that was measured, which was either the pump (PUMP), the first Stokes (S1), or the second Stokes (S2).

For example in Figure 2a, the red curves correspond to a partial pressure of 200 psig of hydrogen and is varied with an increasing presence of helium to 900 psig. The solid line is the pump wavelength, which steadily grew in the experiment as the partial pressure increased. The dotted line is the S1 which grew steadily, but dropped after 700 psig total cell pressure. The dashed line S2, slowly decreased throughout the experiment. From these results it can be inferred that with an increasing amount of buffer gas will suppress the the second Stokes wavelength and increase the output power of the first Stokes and residual pump wavelengths.

After these tests were completed, it was determined that a pressure combination of 200 psig H_2/600 psig He would be the most efficient (53%). Because 266 nm will hopefully be used for future work, it was important to maintain some residual amount of the transmitted pump beam. A similar process was completed for the deuterium cell, which the pressure combination of 300 psig D_2/500 psig He would be the most efficient (27%). The difference in these two efficiencies can be largely attributed to the fact that the hydrogen Raman scattering cross section, $(\frac{d\sigma}{d\omega})$ from (8), is almost twice as large as the deuterium scattering cross section.

3.3 System Description

The schematic of the GSFC TROPOZ DIAL system with the hydrogen (H_2) and deuterium (D_2) Raman cells installed in a portable 13 m trailer is depicted in Figure 3 and an image of the trailer is in Figure 4 below. Lidar systems have been shown to produce comparable results in mobile units as compared to traditional stationary laboratories, but have the advantage of being transported if an event of interest arises (McGee et al. (1991)).

A Spectra Physics Quanta-Ray pulsed Nd:YAG laser has been optimized with two independent parallel laser cavities. These are each comprised of an oscillator/preamplifier with 10 mm YAG rods, followed by two power amplifiers. The beams then pass through potassium dideuterium phosphate (KD*P) crystals. This non-linear optic medium serves the purpose of generating the second and fourth harmonics of the fundamental Nd:YAG frequency. The laser has been optimized for the conversion of the fundamental to the fourth harmonic at a wavelength of 266 nm. These initial pump beams are each approximately 9.6 mm in diameter with a beam divergence of 0.42 mrad.

The two emitted beams are each steered to the Raman cells using two turning mirrors which have been coated to optimize reflectance at 266 nm. The beams pass through converging lenses (L1, L2), with focal length 1.0 m, which fo-

cus each beam waist near the center of the 1.8 m long Raman cells. By focusing the beam waist near the center of the Raman cell, the optical interaction volume is maximized which will give the highest possible conversion of pump photons into 1st Stokes shift photons (McDermid et al. (2002)).

Both ends of the Raman cells are sealed with sapphire optical windows 1.2 cm thick and 3.8 cm in diameter; the flanges used to hold these optics allow for a final optical aperture of 2.2 cm. The sapphire was chosen in preference over fused silica as the window optical material because it is more thermally and mechanically durable under conditions of continuous laser illumination. After the beams exit the Raman cell they are collimated with a 1.0 m re-collimating lens (L3,L4) to minimize beam divergence. The beams are then steered and transmitted through the hatch (90 cm x 92 cm) of the trailer and into the atmosphere.

The GSFC TROPOZ DIAL has a large 45 cm diameter Newtonian telescope for detecting 289/299 nm at higher altitudes (High) in the free troposphere and four smaller 2.5 cm telescopes to obtain signal near the surface (Middle, Low) for 289/299 nm (McGee et al. (2005)). For the 45 cm telescope, the lidar return is focused at the field stop with a 1.0 mrad aperture, which defines the field of view (FOV) of the telescope. The 2.5 cm telescopes have a much wider FOV, 4.5 mrad, which can accommodate the large dynamic range of the Rayleigh backscattered laser light in the near field. There are very narrow band ($<$1.0 nm FWHM) interference filters (IF 289,IF 299) in front of all of the detectors to enhance the amount of usable signal and decrease the amount of ambient background light. These filters are critical to the system because they are spectrally narrow enough for signal detection during the daytime, when tropospheric ozone is most active. After the backscattered light passes through the interference filters it is detected by photomultiplier tubes (PMTs). Neutral density filters have been placed to avoid saturation of the PMTs. Electronic gates are also used on the PMTs to avoid saturation.

Individual photons are counted by a transient recorder (LICEL TR 20 - 80, GmbH, Germany) at a maximum counting rate of 300 MHz. This process is controlled by LabView software which was originally developed for use in other NASA lidar instruments and modified to fit the needs of the GSFC TROPOZ DIAL. The system is triggered via delay generators to interleave the two laser pulses (10 ms offset) to reduce crosstalk between the two channels, which has been shown to decrease electrical system noise in the signal by shifting the timing of this noise beyond the temporal region of data acquisition. All of the important specifications for hardware for each altitude and wavelength channel are listed in Table 2.

The large 45 cm telescope is mounted so that its axis of direction is fixed and can be re-directed only by raising and lowering the hydraulic legs of the trailer. The small 2.5 cm telescopes, however, are set in adjustable mounts so that they can each be directed independently. The alignment of the system is accomplished by steering the outgoing beams into the region of the 45 cm telescope's FOV and optimizing the return signals in the channels associated with this telescope. Optimizing these signals entails maximizing the signal level in the far field. After this alignment is achieved, the axial directions of each of the four smaller telescopes are adjusted so that the return signals associated with them are optimized in the same manner as described for the large telescope. This process has been done during cloud free nighttime hours to minimize solar background and potential contamination of clouds and interfering gases. Geometrically, the 45 cm telescope should be fully overlapped at 462 m AGL and the 2.5 cm telescopes should be fully overlapped at 105 m AGL.

4 Data Processing and Algorithm

The data acquisition system in the GSFC TROPOZ DIAL collects 20 second (1000 laser shots) integrations of the detected backscattered light. This is a low enough temporal resolution to make the assumption of a homogeneous atmosphere during the time of each individual profile. These 20 second integrated profiles will be referred to as the raw signal in this paper. To obtain quality data from these raw signals, the two output pulses from the laser have been interleaved to prevent crosstalk and potential electronic noise, which can contaminate the first few range bins of the retrieval. Interleaving the pulses also puts an offset into the system that must be accounted for. This offset is important because of the sensitivity of the DIAL equation (5) in the retrieval near the surface. This offset was empirically determined using a photodiode and an oscilloscope, but is also shown to be correct in the final retrieved results.

Due to the dynamic nature within the PBL and lower free troposphere, it may be necessary to resolve fine scale mixing features or a layer of ozone aloft at an upper altitude. Depending on the research application, the temporal resolution is selected and the raw data sets are averaged and is defined by the number of data sets that are averaged. For example, a 10 minute temporal resolution corresponds to the running average of 30 raw signal datasets. The time averaged data is then background subtracted using altitudes where the slope of the background is close to zero, in order to assume a linear background correction. This region is typically greater than 30 km.

After these corrections, it may be necessary to manually remove data sets if they are believed to be contaminated by clouds, which is typically quantified by a large rise in luminosity counts at specific altitudes in the individual detectors. If the cloud optical thickness is fairly low and multiple data sets are averaged together, information may be available above the cloud layer.

The retrieval algorithm must also correct for the nonparalyzable dead time correction of the photomultiplier tubes (Keckhut et al. (2004)), which has been empirically determined to be between 4 and 7 ns for most lidar return sig-

nals. These values are quantified by comparing the lidar return signal to a model atmosphere from a standard model or co-located sonde data in the Low channels. Subsequent lidar returns from the Middle and High channels are then corrected to match the overlapping regions of the Low signal returns. This correction can be written as,

$$C_t = \frac{C_m}{1 - C_m T_d}, \tag{9}$$

where the true photon count rate (C_t) can be expressed as a function of the measured count rates (C_M) and a dead time (T_d) parameter (Lampton and Bixler (1985)). This correction is critical in the Low channels where the PMT signals cover a large dynamic range and the derivative in the DIAL equation is large. Signal Induced Bias (SIB) is also quantified, but the channel merge altitudes are selected in a way such that SIB is not a dominant correction.

Referring to equation (5), the retrieval relies on the derivative of the natural logarithm of the ratio of backscattered laser powers. The finite impulse response (FIR) Savitsky-Golay (SG) differentiation filter has been used to produce the required first order derivative. The SG filter is a generalized running average with filter coefficients determined by an unweighted linear least-squares regression and a 2nd order polynomial model applied to the derivative. The second order was chosen instead of a third or fourth order because it was less likely to pick up extreme noise in the derivative. The final vertical resolution of the data is determined using the full width at half maximum (FWHM) of the steady state SG filter coefficients associated with the filter window size.

Due to a known temperature dependence of the ozone absorption cross sections (Figure 1, Malicet et al. (1995)), it is necessary to get an accurate atmospheric temperature profile, either from a co-located sonde launch of from a standard model atmosphere. Because the ozone absorption temperature dependence is not known continuously, a 2nd order polynomial interpolation is utilized. The Rayleigh molecular extinction coefficients are also corrected for atmospheric number density values provided or derived from a co-located sonde launch or from a standard model. After these corrections are made, the first estimate of the ozone profile, $N_{O_3}(r)_1$, is computed.

It is necessary to correct the computed ozone profile in instances of strong aerosol influence, which are particularly prevalent within the PBL. The aerosol extinction term in equation (7) depends not only on the wavelength of the interacting photons, but also on the aerosol size and type. To quantify this, an iterative algorithm has been used to determine the aerosol backscatter coefficient, which when coupled with an assumed lidar ratio, will yield an estimate of the aerosol extinction coefficient. The lidar ratio, S, is the extinction to backscatter ratio,

$$S = \alpha(r)/\beta(r). \tag{10}$$

This procedure, which utilizes the offline, less absorbing wavelength of 299 nm, begins with an initial estimate of the aerosol volume backscatter at a reference height (h_{ref}) and constant lidar ratio which are adapted from Kuang et al. (2011) and Browell et al. (1985).

Rearranging the final DIAL equation (5) with the aerosol correction term, it is possible to solve for the first estimate of the volume backscatter coefficient due to aerosol as,

$$\beta_{aer}(r)_1 = \exp(A+B) \times \frac{r^2(\beta_{mol}(r) + \beta_{aer}(h_{ref}))}{(r+\Delta r)^2} - \beta_{mol}(r) \tag{11}$$

where

$$A = \ln\left(\frac{P_{299}(r+\Delta r)}{P_{299}(r)}\right) \tag{12}$$

and

$$B_i = -2N_{O_3}(r)_i \sigma_{O_3} \Delta r - 2\Delta r(\alpha_{mol}(r) - S\beta_{aer}(h_{ref})). \tag{13}$$

The previously obtained non-aerosol corrected ozone number density, $N_{O_3}(r)_1$, is used for the first guess of the ozone profile in order to calculate B_1. The remaining molecular components are calculated from a standard model atmosphere or from a recent sonde launch. The aerosol backscatter coefficient at the reference height that is used is $\beta_{aer}(h_{ref}) = 1.67 \times 10^{-4} m^{-1} sr^{-1}$, h_{ref} is 12 km and the lidar ratio is assumed to be $S = 60 sr^{-1}$. At this point, equation (11) has been solved for the first complete profile of the aerosol backscatter coefficient, $\beta_{aer}(r)_1$.

For the second iteration, a more accurate value of the aerosol backscatter coefficient can be computed by making the substitution of

$$S\beta_{aer}(h_{ref}) = S(\beta_{aer}(r)_1 + \beta_{aer}(r+\Delta r)_1)/2. \tag{14}$$

This can be solved for the new aerosol backscatter coefficient, $\beta_{aer}(r)_2$.

This iterative process continues, making the necessary substitution of

$$\beta_{aer}(r)_{i+1} + \beta_{aer}(r+\Delta r)_{i+1} = \beta_{aer}(r)_i + \beta_{aer}(r+\Delta r)_i, \tag{15}$$

until a stable solution is reached, where the difference in iterations of the profile is negligible. The final aerosol backscatter term is then inserted into the full DIAL equation (6) and (7) for the final corrected ozone mixing ratio profile. In the test case below, the calculated correction in the final reported ozone mixing ratios were <3 ppbv in the Low channels and <1 ppbv in the Middle and High channels.

The final aerosol corrected ozone profile is then joined to form one continuous hybrid profile. The profile join regions are chosen to maximize SNR, which is at its highest in the lower range of each profile and significantly deteriorates at the top range of each profile. With the current configuration for a 10 minute temporal running average and a fixed SG filter window size, the vertical resolution of the Low channels is 275 meters, the Middle channels is 525 meters and the High channels is 750 meters.

5 Comparison with Beltsville, MD Ozonesonde [25 October 2013]

As mentioned before, the Mid-Atlantic region displays a moderate amount of seasonal ozone variability with the highest concentrations occurring in the late July time period (Lehman et al. (2004)). Because of this, during the fall and winter seasons, the TROPOZ focuses its observations on monitoring ozone in the free troposphere and the aforementioned source contributions, such as STE. While taking measurements on 25 October 2013, an unusually low tropopause was observed, resulting in the exchange of high amounts of ozone between the stratosphere and the lower free troposphere. An ozonesonde was launched that day by the Howard University Beltsville Center for Climate Systems Observation, which serves as the validation source for the TROPOZ ozone profiles. The launch site (39.05°N, 76.88°W) is approximately 8 km from the lidar site which is close enough to assume similar, but not identical tropospheric micrometeorology in the dynamic daytime PBL.

A 10-minute retrieved lidar ozone profile (17:44:1754 UTC) together with the ozonesonde profile (17:44 UTC launch) are shown in Figure 5. The retrieved range of the lidar profile is from 400 m to 12 km AGL. Both the lidar and the sonde show a PBL height near 1.5 km which is based on the slight ozone mixing ratio gradient, the strong relative humidity gradient, and the temperature inversion. Above the PBL, both profiles have values in the range 30-40 ppbv until the strong ozone gradient near 6.5 km. Both the sonde and the lidar capture this strong ozone reservoir, where the difference in the altitude of the reservoir may be attributed to the distance between sites based on the fact that the ozonesonde profile still resides within the uncertainty of the retrieved profile. This ozone reservoir, which was around 150-200 ppbv, had a higher ozone mixing ratio than most summer days and previous test cases did not reach these values until 12 km, which emphasizes the regional and seasonal uniqueness of this test case. The uncertainty bars shown in the retrieved TROPOZ ozone profile are dominated by the statistical uncertainty of photon counting and SNR, which are discussed more in Section 6.

The TROPOZ profile differs from the sonde profile above 8 km; an explanation for this can be seen in Figure 6. This image shows the GPS trajectory of the sonde for its first 10 km of ascent overlain on a map of the area. The color of the trajectory track represents the altitude of the sonde. The sonde was launched at Beltsville, MD and was closest to GSFC in the ascent at an altitude near 3 km, which also implies that the difference in ozone mixing ratio in the first 2 km may be due to the distance between sites. As the sonde continued along this trajectory, it entered a marine environment. The eastern end of the trajectory, where the sonde had achieved 10 km altitude, is near Edgewater, MD, nearly 30 km distant from the lidar site. Because the lidar is in an Eulerian frame of reference in the inland urban environment, it was not actually resolving the same air mass that is present at the beginning or end of the Lagrangian frame of reference of the sonde. This highlights one of the inherent complications in using ozonesondes as a validation source for lidar. Because the lidar is stationary, the resolved ozone profiles are more representative of the ozone profile at the observation site.

The ozone mixing ratio, relative humidity and temperature are plotted from the ECC and radiosonde in Figure 7. The ozone mixing ratio is fairly constant in the first 6 km with low variability until the large ozone gradient at 6.5 km. Above that point there are large oscillations that imply a dynamic system of ozone in this region. The relative humidity profile shows a strong gradient at the top of the PBL but above that the air slowly gets drier until about 6.5 km where it also undergoes a strong gradient. The relative humidity also shows some small oscillations that correspond to the same altitudes as the dynamic ozone oscillations. The temperature profile exhibits a linear decrease up to 6.5 km above which the temperature remains nearly constant for 2 km. This, together with the observation of a dry air mass above 6.5 km, indicate an unusually low tropopause height near 6.5 km. This implies that this air mass is most likely of stratospheric origin and can be considered an ozone intrusion event and can be classified as STE (Reiter (1975)).

A 500-millibar (mb) height contour national map for 11:00 UTC 25 October 2013, courtesy NOAA Daily Weather Map, for the meteorological events that surrounded the test case is shown in Figure 8. The chart shows height contours (solid lines), temperatures (dashed lines) and winds (arrows). The height contours show the height of the 500-mb pressure level in dekameters above sea level, the isotherms, or lines of constant temperature, are shown in degrees Celsius, and the arrows show the wind direction and speed at the 500-mb level. The map shows a persistent low pressure system occurring in the Mid-Atlantic and Ohio River Valley regions just underneath the tropopause height around 6.5 km. This disturbance is exemplified by the deviation from the trough of closely spaced geopotential height contours (solid black lines) and in the temperature contours (dashed black lines). Also, notice the strong increase in northwesterly winds associated with the steep pressure gradients that have occurred just below the tropopause around 6.5 km. This wind pattern is most likely the Polar jet stream (Viezee et al. (1983)), which is typically stronger in winter and fall months and was the reason why

the ozonesonde in Figure 6 moved so quickly in the zonal direction away from the launch site as it got nearer to the tropopause height. The low pressure system was present in national maps as early as 23:00 UTC 24 October 2013 and slowly subsided and evolved throughout 25 October 2013 as can be seen in the lidar curtain plots in Figure 9a and 9b.

Figure 9a shows the time series from 15:19-22:18 UTC (11:19 - 18:18 EST) with the overlaid ozonesonde data corresponding to the red arrow point at 17:44 UTC. This image is created from a 10 minute running average of the data with all altitude channels merged together to form a complete profile of the atmosphere from 400 meters to 12 km. It is possible to see the strong gradient in ozone near 7 km and large ozone concentrations that dissipate mainly through titration during the afternoon and early evening. The upper level cold and dry air pockets behind the persistent low pressure system inject a large ozone reservoir (150-200 ppbv) into the free troposphere, effectively lowering and maintaing a tropopause height near 6.5 km. The in situ surface ozone mixing ratios from the GSFC TROPOZ DIAL trailer (Thermo Scientific 49i, 1 minute resolution) are reported in the first bin in the time series below the retrievable altitude. These values range from 18-24 ppbv at the surface for the entire experiment, which implies at ground level the ozone was behaving like a typical early winter Mid-Atlantic regional atmosphere. Based on the northwest direction and strong wind speeds shown in Figure 8, there was dilution and ventilation of ozone precursors which resulted in a low amount of of ozone near the surface from local pollution.

Around 19:00 and 21:00 UTC, thin clouds drifted through the field of view during the observation, the effects of which can be seen as white space in the figure. Because the 10 minute observation is a running average over 30 profiles, and because the clouds were thin and did not form broad cover, retrieval information can be seen above the clouds in the curtain plot.

The curtain plot in Figure 9b shows the same data set with a temporal resolution of 1 minute from 4 to 10 km. This is a high enough resolution to begin to pick out some of the small scale features in the ozone curtain plot. With an running average of just 3 profiles, retrieval above the clouds is lost, hence, the vertical white lines that appear in Figure 9b. Averaging less profiles does increase the uncertainty in the measurement and the retrieved ozone profile at 1 minute resolution can only reach 10 km (as opposed to 12 km with a 10 minute resolution) before the SNR is too small yield useful information.

This plot focuses attention on the upper atmospheric conditions in order to represent the ability to monitor the changing dynamics of the ozone reservoir on a very short time scale. It is possible to see small pockets of clean air which implies that there was some dynamic mixing of clean tropospheric air and high ozone stratospheric air. There is also an interesting wavelike feature in the ozone concentration towards the end of the run (20:30-22:18 at 6.5 km) that may have been the cause for the ozone reservoir to split and begin to both subside towards the surface and to rise back to the upper free troposphere. The ozone free region between two ozone enhanced layers is certainly characteristic of a tropopause fold event (Viezee et al. (1983)), but without the meteorological parameters from a radiosonde, it is difficult to confirm the fold. Dilution of this ozone may have occurred in the atmosphere during the times at which the TROPOZ was not taking measurements, especially with high winds pushing the air mass out towards the Chesapeake Bay.

Surface monitors did show an increase in ozone on 26 October 2013; but, with the passing front bringing warm, sunny weather, it is challenging to determine whether the surface ozone source was due to the dynamic STE or created by photochemistry within the PBL.

Due to the unusually high amount of ozone in the atmosphere during this test case, the usable return signal was absorbed much more strongly than a typical day. Because of this, ozone mixing ratios are only reported to 12 km. For conditions of nighttime observations and longer temporal averages, ozone retrievals can be attained at a higher altitude. Although this plot emphasizes the upper atmospheric conditions for this regionally important test case, it provides evidence that the GSFC TROPOZ DIAL will be able to provide high resolution ozone observations within the dynamic PBL.

6 Accuracy of the DIAL measurement

The GSFC TROPOZ DIAL system detects individual photons through the use of photomultiplier tubes. The signal collected by these PMTs follows Poisson statistics (Megie et al. (1985), Papayannis et al. (1990)) and the statistical uncertainty of the ozone number density can be calculated as

$$\epsilon_{N_{o3}}(r) = \frac{1}{2N_{o3}\Delta\sigma_{O_3}\Delta r}\sqrt{\frac{P_{s,\lambda}+P_{b,\lambda}+P_{d,\lambda}}{P_{s,\lambda}^2}}, \qquad (16)$$

where $P_{s,\lambda}$, $P_{b,\lambda}$, and $P_{d,\lambda}$ are the atmospheric backscattered signal, background radiation, and dark counts of the detector at wavelength λ. The vertical resolution, which is based on the SG filter window size, is denoted as Δr and the differential ozone absorption cross section is denoted as $\Delta\sigma_{O_3}$. The statistical uncertainty is related to the square root of the total PMT counts, both those that are relevant to the retrieval of ozone number density and those that are counts due to systematic uncertainties. By integrating profiles for a longer duration, the backscattered signal term $P_{s,\lambda}$ becomes much larger than the $P_{b,\lambda}$ and $P_{d,\lambda}$ terms. For this reason, the temporal resolution is inherently built into the statistical uncertainty of the system and averaging many data sets is beneficial to the resultant uncertainty in the system.

By increasing the vertical resolution of the profile, which is in the denominator of equation 16, the statistical uncertainty in the measurement decreases. Because the vertical

resolution changes with the retrieval range and has different values for different channel pairs, the resultant uncertainty profile exhibits changes at the altitudes at which the channels are merged. This can be seen in the uncertainty bars in Figure 5.

Aside from the statistical uncertainty, there are uncertainties associated with the spectral dependence of other interfering species, such as aerosols, non-ozone interfering gases, and the Rayleigh atmosphere. As mentioned in the Data Processing portion of this paper, an iterative aerosol correction was applied to this test case, which resulted in a $<$3 ppbv ($<$12%) ozone correction in the Low channels and a $<$1 ppbv ($<$4%) correction in the Middle and High channels.

Further uncertainties arise from interfering gases that have similar absorption cross sections at the DIAL wavelengths (Keckhut et al. (2004)). An uncertainty of 1.5% in overall retrieved ozone has been calculated due to absorption at the DIAL wavelengths by the oxygen dimer (O2-O2) interaction (Fally et al. (2000)), a -1.0% uncertainty due to sulfur dioxide (SO2) (Stark et al. (1999)), and a -0.5% uncertainty due to nitrogen dioxide (NO_2)(Bogumil et al. (2003)). The uncertainty in the Rayleigh extinction correction is typically $<$1% due to the dependence on the atmospheric number density, which may be calculated from a standard model atmosphere or recent radiosonde. Similarly, the temperature dependence of the ozone absorption cross sections should contribute less than 3% to the uncertainty in the final ozone number density (Leblanc et al. (1998)).

Table 3 lists the various uncertainties due to individual photon counting, interfering gases, the temperature dependence of the ozone cross section, and the saturation correction for the test case discussed in the previous section. Other than the uncertainty due to the presence of aerosols, and to a lesser extent those due to Rayleigh extinction and saturation correction, these values can be taken as representative of the uncertainties in ozone retrieval for the GSFC TROPOZ DIAL instrument. The uncertainties are largest in the Low channel due to the presence of aerosols and the complete use of the saturation correction. In the Middle and High channels, there are fewer aerosols present and there is enough overlap between the Low and Middle and between the Middle and High channels to join them at altitudes such that regions where saturation is non-negligible can be excluded from the overall profile. The reported resultant uncertainty, added in quadrature, from 0-1.5 km is 16-19%, 1.5 -3 km is 10 - 18%, and from 3 km to 12 km is 11 - 25%.

7 Conclusions

The GSFC TROPOZ DIAL has been utilized to detect tropospheric ozone, a very important greenhouse gas for climate and health studies. Due to complex tropospheric chemistry and various free tropospheric ozone sources, modeling these lower levels of the atmosphere can be extremely difficult and empirical observations of ozone may be far more useful. The necessary theory and initial optical layout of the GSFC TROPOZ DIAL in order to retrieve and better characterize the vertical distribution of tropospheric ozone in the Baltimore-Washington D.C. area has been established. A regionally important validation test case of an unusually low tropopause, resulting in the exchange of high amounts of ozone between the stratosphere and the lower free troposphere, or STE, is presented and analyzed.

Measurements of the STE are presented with a temporal resolution of 10 minutes and 1 minute with a maximum altitude of 12 km. Because of the optically thick stratospheric ozone layer, a ground based detection method, which can detect tropospheric ozone on a continuous, high resolution scale is advantageous. The GSFC TROPOZ DIAL system has shown to be a less expensive and more robust alternative to previous lidar systems with the implementation of Raman cells, which have had no observable drop in pressure since they were initially filled in June 2013. The data processing algorithm has been introduced and has shown to have agreement with a co-located ozonesonde measurement. The reported resultant uncertainty from 0-1.5 km is 16-19%, 1.5 -3 km is 10 - 18%, and from 3 km to 12 km is 11 - 25%.

Future plans for the GSFC TROPOZ DIAL are to obtain ozone profiles as close to the surface as possible ($<$ 100 m AGL), which may be obtainable with ozonesonde launches directly at the lidar site. As mentioned previously, the Raman cells were filled to a pressure which left a residual amount of 266 nm for atmospheric transmission. Because this wavelength is strongly absorbed by ozone it may only be able to yield useful information from the surface to the top of the PBL, but may have enough signal to characterize and probe the dynamic PBL. The advantage of adding 266 nm to this system would be to get a more robust aerosol correction method using a dual-DIAL wavelength retrieval.

Depending on the atmospheric event the system is intended to monitor, averaging of the data may be minimized to detect natural variability and small ozone fluctuations or maximized to reach higher altitudes for climatology purposes. The GSFC TROPOZ DIAL is a new and unique tool for the air quality community in the Baltimore-Washington D.C. region because it can provide a continuous, high resolution and novel perspective of ozone pollution episodes. For these reasons, the GSFC TROPOZ DIAL is a very valuable instrument for quantifying the vertical distribution of ozone, especially for distinguishing layers of ozone aloft and STE events that surface monitors do not have the ability to detect.

Acknowledgements. The authors wish gratefully to acknowledge support for this study provided from UMBC/JCET (Task #374, Project 8306), the Maryland Department of the Environment (MDE, Contract #U00P4400079), NOAA-CREST CCNY Foundation (Sub-Contract #49173B-02) and the Tropospheric Ozone Lidar Network (TOLNet). Also, thanks to the Howard University

Beltsville Center for Climate Systems Observation for launching the ozonesondes necessary to begin validating this system.

References

Alvarez, R. J., Senff, C. J., Langford, A. O., Weickmann, A. M., Law, D. C., Machol, J. L., Merritt, D. A., Marchbanks, R. D., Sandberg, S. P., Brewer, W. A., Hardesty, R. M., and Banta, R. M.: Development and Application of a Compact, Tunable, Solid-State Airborne Ozone Lidar System for Boundary Layer Profiling, Journal of Atmospheric and Oceanic Technology, 28, 1258–1272, 2011.

Ancellet, G. and Ravetta, F.: Compact Airborne Lidar for Tropospheric Ozone: Description and Field Measurements, Appl. Opt., 37, 5509–5521, http://ao.osa.org/abstract.cfm?URI=ao-37-24-5509, 1998.

Banta, R. M., Senff, C. J., Nielsen-Gammon, J., Darby, L. S., Ryerson, T. B., Alvarez, R. J., Sandberg, S. P., Williams, E. J., and Trainer, M.: A Bad Air Day in Houston, Bulletin of the American Meteorological Society, 86, 657–669, 2005.

Bogumil, K., Orphal, J., Homann, T., Voigt, S., Spietz, P., Fleischmann, O., Vogel, A., Hartmann, M., Kromminga, H., Bovensmann, H., Frerick, J., and Burrows, J.: Measurements of molecular absorption spectra with the {SCIAMACHY} pre-flight model: instrument characterization and reference data for atmospheric remote-sensing in the 230–2380 nm region, Journal of Photochemistry and Photobiology A: Chemistry, 157, 167 – 184, 2003.

Bösenberg, J.: Ground-Based Differential Absorption Lidar for Water-Vapor and Temperature Profiling: Methodology, Appl. Opt., 37, 3845–3860, 1998.

Bowman, K. W., Steck, T., Worden, H. M., Worden, J., Clough, S., and Rodgers, C.: Capturing time and vertical variability of tropospheric ozone: A study using TES nadir retrievals, Journal of Geophysical Research: Atmospheres, 107, ACH 21–1–ACH 21–11, http://dx.doi.org/10.1029/2002JD002150, 2002.

Browell, E.: Differential absorption lidar sensing of ozone, Proceedings of the IEEE, 77, 419–432, 1989.

Browell, E. V., Wilkerson, T. D., and Mcilrath, T. J.: Water vapor differential absorption lidar development and evaluation, Appl. Opt., 18, 3474–3483, http://ao.osa.org/abstract.cfm?URI=ao-18-20-3474, 1979.

Browell, E. V., Carter, A. F., Shipley, S. T., Allen, R. J., Butler, C. F., Mayo, M. N., Jr, J. H. S., and Hall, W. M.: NASA multipurpose airborne DIAL system and measurements of ozone and aerosol profiles, Appl. Opt., 22, 522–534, http://ao.osa.org/abstract.cfm?URI=ao-22-4-522, 1983.

Browell, E. V., Ismail, S., and Shipley, S. T.: Ultraviolet DIAL measurements of O3 profiles in regions of spatially inhomogeneous aerosols, Appl. Opt., 24, 2827–2836, http://ao.osa.org/abstract.cfm?URI=ao-24-17-2827, 1985.

Browell, E. V., Danielsen, E. F., Ismail, S., Gregory, G. L., and Beck, S. M.: Tropopause fold structure determined from airborne lidar and in situ measurements, Journal of Geophysical Research: Atmospheres, 92, 2112–2120, http://dx.doi.org/10.1029/JD092iD02p02112, 1987.

Browell, E. V., Butler, C. F., Fenn, M. A., Grant, W. B., Ismail, S., Schoeberl, M. R., Toon, O. B., Loewenstein, M., and Podolske, J. R.: Ozone and Aerosol Changes During the 1991-1992 Airborne Arctic Stratospheric Expedition, Science, 261, 1155–1158, http://www.sciencemag.org/content/261/5125/1155.abstract, 1993.

Carlsten, J. L., Telle, J. M., and Wenzel, R. G.: Efficient stimulated Raman scattering due to absence of second Stokes growth, Opt. Lett., 9, 353–355, http://ol.osa.org/abstract.cfm?URI=ol-9-8-353, 1984.

Delgado, R., Rabenhorst, S., Demoz, B., and Hoff, R.: Elastic lidar measurements of summer nocturnal low level jet events over Baltimore, Maryland, Journal of Atmospheric Chemistry, pp. 1–23, http://dx.doi.org/10.1007/s10874-013-9277-2, 2014.

Demerjian, K. L.: A review of national monitoring networks in North America, Atmospheric Environment, 34, 1861 – 1884, http://www.sciencedirect.com/science/article/pii/S1352231099004525, 2000.

Dion, P. and May, A. D.: Motional Narrowing and Other Effects in the Q Branch of HD, Canadian Journal of Physics, 51, 36–39, http://www.nrcresearchpress.com/doi/abs/10.1139/p73-005, 1973.

Duncan, M. D., Mahon, R., Reintjes, J., and Tankersley, L. L.: Parametric Raman gain suppression in D2 and H2, Opt. Lett., 11, 803–805, http://ol.osa.org/abstract.cfm?URI=ol-11-12-803, 1986.

Fally, S., Vandaele, A., Carleer, M., Hermans, C., Jenouvrier, A., Mérienne, M.-F., Coquart, B., and Colin, R.: Fourier Transform Spectroscopy of the O2 Herzberg Bands. III. Absorption Cross Sections of the Collision-Induced Bands and of the Herzberg Continuum, Journal of Molecular Spectroscopy, 204, 10 – 20, http://www.sciencedirect.com/science/article/pii/S0022285200982043, 2000.

Falsini, P., Pini, R., Salimbeni, R., Vannini, M., Haider, A., and Buffa, R.: Simple and efficient H2 Raman conversion of a XeCl laser with a variable numerical aperture coupling geometry, Optics Communications, 53, 421 – 424, http://www.sciencedirect.com/science/article/pii/0030401885900318, 1985.

Fishman, J., Watson, C. E., Larsen, J. C., and Logan, J. A.: Distribution of tropospheric ozone determined from satellite data, Journal of Geophysical Research: Atmospheres, 95, 3599–3617, http://dx.doi.org/10.1029/JD095iD04p03599, 1990.

Haner, D. and McDermid, I.: Stimulated Raman shifting of the Nd:YAG fourth harmonic (266 nm) in H2, HD, and D2, Quantum Electronics, IEEE Journal of, 26, 1292 –1298, 1990.

IPCC: Climate Change 2007 - The Physical Science Basis: Working Group I Contribution to the Fourth Assessment Report of the IPCC, Climate Change 2007, Cambridge University Press, 2007.

Keckhut, P., McDermid, S., Swart, D., McGee, T., Godin-Beekmann, S., Adriani, A., Barnes, J., Baray, J.-L., Bencherif, H., Claude, H., di Sarra, A. G., Fiocco, G., Hansen, G., Hauchecorne, A., Leblanc, T., Lee, C. H., Pal, S., Megie, G., Nakane, H., Neuber, R., Steinbrecht, W., and Thayer, J.: Review of ozone and temperature lidar validations performed within the framework of the Network for the Detection of Stratospheric Change, J. Environ. Monit., 6, 721–733, http://dx.doi.org/10.1039/B404256E, 2004.

Komhyr, W. D., Barnes, R. A., Brothers, G. B., Lathrop, J. A., and Opperman, D. P.: Electrochemical concentration cell ozonesonde performance evaluation during STOIC 1989, Journal of Geophysical Research: Atmospheres, 100, 9231–9244, http://dx.doi.org/10.1029/94JD02175, 1995.

Komine, H.: Stimulated vibrational Raman scattering in HD, Quantum Electronics, IEEE Journal of, 22, 520–521, 1986.

Kovalev, V. A. and Eichinger, W. E.: Elastic Lidar: Theory, Practice, and Analysis Methods, Wiley-Interscience, 1 edn., 2004.

Kuang, S., Burris, J., Newchurch, M., Johnson, S., and Long, S.: Differential Absorption Lidar to Measure Subhourly Variation of Tropospheric Ozone Profiles, Geoscience and Remote Sensing, IEEE Transactions on, 49, 557 –571, 2011.

Kuang, S., Newchurch, M. J., Burris, J., and Liu, X.: Ground-based lidar for atmospheric boundary layer ozone measurements, Appl. Opt., 52, 3557–3566, http://ao.osa.org/abstract.cfm?URI=ao-52-15-3557, 2013.

Lampton, M. and Bixler, J.: Counting efficiency of systems having both paralyzable and nonparalyzable elements, Review of Scientific Instruments, 56, 164–165, http://link.aip.org/link/?RSI/56/164/1, 1985.

Langford, A. O.: Stratosphere-troposphere exchange at the subtropical jet: Contribution to the tropospheric ozone budget at mid-latitudes, Geophysical Research Letters, 26, 2449–2452, http://dx.doi.org/10.1029/1999GL900556, 1999.

Langford, A. O., Senff, C. J., Alvarez, R. J., Banta, R. M., and Hardesty, R. M.: Long-range transport of ozone from the Los Angeles Basin: A case study, Geophysical Research Letters, 37, L0687, http://dx.doi.org/10.1029/2010GL042507, 2010.

Leblanc, T., McDermid, I. S., Hauchecorne, A., and Keckhut, P.: Evaluation of optimization of lidar temperature analysis algorithms using simulated data, Journal of Geophysical Research: Atmospheres, 103, 6177–6187, http://dx.doi.org/10.1029/97JD03494, 1998.

Lehman, J., Swinton, K., Bortnick, S., Hamilton, C., Baldridge, E., Eder, B., and Cox, B.: Spatio-temporal characterization of tropospheric ozone across the eastern United States, Atmospheric Environment, 38, 4357 – 4369, http://www.sciencedirect.com/science/article/pii/S1352231004003838, 2004.

Malicet, J., Daumont, D., Charbonnier, J., Parisse, C., Chakir, A., and Brion, J.: Ozone UV spectroscopy. II. Absorption cross-sections and temperature dependence, Journal of Atmospheric Chemistry, 21, 263–273, http://dx.doi.org/10.1007/BF00696758, 1995.

McDermid, I. S., Haner, D. A., Kleiman, M. M., Walsh, T. D., and White, M. L.: Differential absorption lidar systems for tropospheric and stratospheric ozone measurements, Optical Engineering, 30, 22–30, http://dx.doi.org/10.1117/12.55768, 1991.

McDermid, I. S., Beyerle, G., Haner, D. A., and Leblanc, T.: Redesign and improved performance of the tropospheric ozone lidar at the jet propulsion laboratory table mountain facility, Appl. Opt., 41, 7550–7555, http://ao.osa.org/abstract.cfm?URI=ao-41-36-7550, 2002.

McDonnell, W. F., Abbey, D. E., Nishino, N., and Lebowitz, M. D.: Long-Term Ambient Ozone Concentration and the Incidence of Asthma in Nonsmoking Adults: The Ahsmog Study, Environmental Research, 80, 110 – 121, http://www.sciencedirect.com/science/article/pii/S0013935198938944, 1999.

McGee, T. J., Whiteman, D. N., Butler, J. J., Burris, J. F., and Ferrare, R. A.: STROZ LITE: Stratospheric Ozone Lidar Trailer Experiment, Optical Engineering, 30, 31–39, http://dx.doi.org/10.1117/12.55771, 1991.

McGee, T. J., Gross, M., Ferrare, R., Heaps, W., and Singh, U.: Raman dial measurements of stratospheric ozone in the presence of volcanic aerosols, Geophysical Research Letters, 20, 955–958, http://dx.doi.org/10.1029/93GL00751, 1993.

McGee, T. J., Gross, M. R., Singh, U. N., Butler, J. J., and Kimvilakani, P. E.: Improved stratospheric ozone lidar, Optical Engineering, 34, 1421–1430, http://dx.doi.org/10.1117/12.199883, 1995.

McGee, T. J., Twigg, L., Hoegy, W., Burris, J. F., Heaps, W. S., Sumnicht, G., and Hostetler, C. A.: AROTAL: results from two arctic campaigns, Proc. SPIE, 5653, 121–129, http://dx.doi.org/10.1117/12.578959, 2005.

Measures, R. M.: Laser Remote Sensing: Fundamentals and Applications, Wiley, New York, 1983.

Megie, G. J., Ancellet, G., and Pelon, J.: Lidar measurements of ozone vertical profiles, Appl. Opt., 24, 3454–3463, http://ao.osa.org/abstract.cfm?URI=ao-24-21-3454, 1985.

Menzies, R. T. and Shumate, M. S.: Tropospheric ozone distributions measured with an airborne laser absorption spectrometer, Journal of Geophysical Research: Oceans, 83, 4039–4043, http://dx.doi.org/10.1029/JC083iC08p04039, 1978.

Middleton, W. E. K. and Spilhaus, A. F.: Meteorological Instruments. University of Toronto Press. 3rd Edition, Quarterly Journal of the Royal Meteorological Society, 80, 484, http://dx.doi.org/10.1002/qj.49708034532, 1953.

Milton, M. J. T. and Woods, P. T.: Pulse averaging methods for a laser remote monitoring system using atmospheric backscatter, Appl. Opt., 26, 2598–2603, http://ao.osa.org/abstract.cfm?URI=ao-26-13-2598, 1987.

Mollenauer, L., White, J., and Pollock, C.: Stimulated Raman scattering, vol. 59 of *Topics in Applied Physics*, Springer Berlin Heidelberg, http://dx.doi.org/10.1007/3-540-55571-4_4, 1992.

Morris, G. A., Ford, B., Rappenglück, B., Thompson, A. M., Mefferd, A., Ngan, F., and Lefer, B.: An evaluation of the interaction of morning residual layer and afternoon mixed layer ozone in Houston using ozonesonde data, Atmospheric Environment, 44, 4024 – 4034, http://www.sciencedirect.com/science/article/pii/S1352231009005032, 2010.

Murray, E. R., Powell, D. D., and van der Laan, J. E.: Measurement of average atmospheric temperature using a CO2 laser radar, Appl. Opt., 19, 1794–1797, http://ao.osa.org/abstract.cfm?URI=ao-19-11-1794, 1980.

Murray, J. and Javan, A.: Effects of collisions on Raman line profiles of hydrogen and deuterium gas, Journal of Molecular Spectroscopy, 42, 1 – 26, http://www.sciencedirect.com/science/article/pii/0022285272901397, 1972.

NCADAC: The National Climate Assessment and Development Advisory Committee (NCADAC) Draft Climate Assessment Report, http://ncadac.globalchange.gov/, 2013.

Newchurch, M. J., Ayoub, M. A., Oltmans, S., Johnson, B., and Schmidlin, F. J.: Vertical distribution of ozone at four sites in the United States, Journal of Geophysical Research: Atmospheres, 108, ACH 9–1–ACH 9–17, http://dx.doi.org/10.1029/2002JD002059, 2003.

Oltmans, S. J., Levy, H., Harris, J. M., Merrill, J. T., Moody, J. L., Lathrop, J. A., and Cuevas, E.: Summer and spring ozone profiles over the North Atlantic from ozonesonde measurements, Journal of Geophysical Research: Atmospheres, 101, 29 179–29 200, http://dx.doi.org/10.1029/96JD01713, 1996.

Papayannis, A., Ancellet, G., Pelon, J., and Mégie, G.: Multiwavelength lidar for ozone measurements in the troposphere and the

lower stratosphere, Appl. Opt., 29, 467–476, http://ao.osa.org/abstract.cfm?URI=ao-29-4-467, 1990.

Proffitt, M. H. and Langford, A. O.: Ground-based differential absorption lidar system for day or night measurements of ozone throughout the free troposphere, Appl. Opt., 36, 2568–2585, http://ao.osa.org/abstract.cfm?URI=ao-36-12-2568, 1997.

Puzak, J. C.: The EPA's Role in the Quality Assurance of Ambient Air Pollutant Measurements, American Society for Testing and Materials (ASTM), 1987.

Reiter, E. R.: Stratospheric-tropospheric exchange processes, Reviews of Geophysics, 13, 459–474, http://dx.doi.org/10.1029/RG013i004p00459, 1975.

Schumann, U. and Huntrieser, H.: The global lightning-induced nitrogen oxides source, Atmospheric Chemistry and Physics, 7, 3823–3907, http://www.atmos-chem-phys.net/7/3823/2007/, 2007.

Senff, C. J., Alvarez, R. J., Hardesty, R. M., Banta, R. M., and Langford, A. O.: Airborne lidar measurements of ozone flux downwind of Houston and Dallas, Journal of Geophysical Research: Atmospheres, 115, D20 307, http://dx.doi.org/10.1029/2009JD013689, 2010.

Shen, Y. R. and Bloembergen, N.: Theory of Stimulated Brillouin and Raman Scattering, Phys. Rev., 137, A1787–A1805, http://link.aps.org/doi/10.1103/PhysRev.137.A1787, 1965.

Stark, G., Smith, P. L., Rufus, J., Thorne, A. P., Pickering, J. C., and Cox, G.: High-resolution photoabsorption cross-section measurements of SO2 at 295 K between 198 and 220 nm, Journal of Geophysical Research: Planets, 104, 16 585–16 590, http://dx.doi.org/10.1029/1999JE001022, 1999.

Stevenson, D. S., Young, P. J., Naik, V., Lamarque, J.-F., Shindell, D. T., Voulgarakis, A., Skeie, R. B., Dalsoren, S. B., Myhre, G., Berntsen, T. K., Folberth, G. A., Rumbold, S. T., Collins, W. J., MacKenzie, I. A., Doherty, R. M., Zeng, G., van Noije, T. P. C., Strunk, A., Bergmann, D., Cameron-Smith, P., Plummer, D. A., Strode, S. A., Horowitz, L., Lee, Y. H., Szopa, S., Sudo, K., Nagashima, T., Josse, B., Cionni, I., Righi, M., Eyring, V., Conley, A., Bowman, K. W., Wild, O., and Archibald, A.: Tropospheric ozone changes, radiative forcing and attribution to emissions in the Atmospheric Chemistry and Climate Model Intercomparison Project (ACCMIP), Atmospheric Chemistry and Physics, 13, 3063–3085, http://www.atmos-chem-phys.net/13/3063/2013/, 2013.

Thompson, A. M., Witte, J. C., Oltmans, S. J., Schmidlin, F. J., Logan, J. A., Fujiwara, M., Kirchhoff, V. W. J. H., Posny, F., Coetzee, G. J. R., Hoegger, B., Kawakami, S., Ogawa, T., Fortuin, J. P. F., and Kelder, H. M.: Southern Hemisphere Additional Ozonesondes (SHADOZ) 1998–2000 tropical ozone climatology 2. Tropospheric variability and the zonal wave-one, Journal of Geophysical Research: Atmospheres, 108, 8241, http://dx.doi.org/10.1029/2002JD002241, 2003.

Thompson, A. M., Yorks, J. E., Miller, S. K., Witte, J. C., Dougherty, K. M., Morris, G. A., Baumgardner, D., Ladino, L., and Rappenglück, B.: Tropospheric ozone sources and wave activity over Mexico City and Houston during MILAGRO/Intercontinental Transport Experiment (INTEX-B) Ozonesonde Network Study, 2006 (IONS-06), Atmospheric Chemistry and Physics, 8, 5113–5125, http://www.atmos-chem-phys.net/8/5113/2008/, 2008.

Uchino, O., Maeda, M., Kohno, J., Shibata, T., Nagasawa, C., and Hirono, M.: Observation of stratospheric ozone layer by a XeCl laser radar, Applied Physics Letters, 33, 807–809, 1978.

U.S. Standard: U.S. standard atmosphere, 1976 / [adopted by the United States Committee on Extension to the Standard Atmosphere], National Oceanic and Amospheric Administration. U.S. Govt. Print. Off., Washington :, 1976.

Viezee, W., Johnson, W. B., and Singh, H. B.: Stratospheric ozone in the lower troposphere—II. Assessment of downward flux and ground-level impact, Atmospheric Environment (1967), 17, 1979 – 1993, http://www.sciencedirect.com/science/article/pii/0004698183903542, 1983.

Weitkamp, C., ed.: Lidar: Range-Resolved Optical Remote Sensing of the Atmosphere, Springer, 2006.

Witkowicz, T. and May, A. D.: Collisional effects in compressed HD, Canadian Journal of Physics, 54, 575–583, http://www.nrcresearchpress.com/doi/abs/10.1139/p76-062, 1976.

Yorks, J. E., Thompson, A. M., Joseph, E., and Miller, S. K.: The variability of free tropospheric ozone over Beltsville, Maryland (39N, 77W) in the summers 2004–2007, Atmospheric Environment, 43, 1827 – 1838, http://www.sciencedirect.com/science/article/pii/S1352231008011436, 2009.

Yuan, T., Remer, L. A., Bian, H., Ziemke, J. R., Albrecht, R., Pickering, K. E., Oreopoulos, L., Goodman, S. J., Yu, H., and Allen, D. J.: Aerosol indirect effect on tropospheric ozone via lightning, J. Geophys. Res., 117, D18 213, http://dx.doi.org/10.1029/2012JD017723, 2012.

Ziemke, J. R., Chandra, S., Duncan, B. N., Froidevaux, L., Bhartia, P. K., Levelt, P. F., and Waters, J. W.: Tropospheric ozone determined from Aura OMI and MLS: Evaluation of measurements and comparison with the Global Modeling Initiative's Chemical Transport Model, Journal of Geophysical Research: Atmospheres, 111, D19 303, http://dx.doi.org/10.1029/2006JD007089, 2006.

Table 1: Vibrational Raman frequencies and first Stokes wavelengths obtained from the stimulated Raman scattering of Nd:YAG fourth harmonic in the Raman active gases. [Source: Measures (1983)]

Select Gas	Vibr. Raman Frequency	1st Stokes
Hydrogen	4160.0 cm^{-1}	299.1 nm
Deuterium	2986.1 cm^{-1}	288.9 nm

Table 2: Hardware Description for the GSFC TROPOZ DIAL system for the transmitter, receiver components and the data aquisiton system.

System Component	299 ("off") Channels	289 ("on") Channels
Wavelength Source	Nd:YAG	Nd:YAG
Pulse Width	8 ns	8 ns
Beam Divergence	0.42 mrad	0.44 mrad
Repetition Rate	50 hz	50 hz
Pump Power	32 mJ/pulse (1.6 W)	42 mJ/pulse (2.1 W)
Raman Cell Partial Pressures [psig]	200 H_2/600 He	300 D_2/400 He
Gas Purities	99.9999 % H_2	99.999 % D_2
Raman Cell Efficiencies	53%	26%
Transmitted Raman Pulse Energy	17 mJ/pulse (0.85 W)	11 mJ/pulse (0.55 W)
Interference Filters	Materion Precision	Materion Precision
Center Wavelengths	299.1 ± 0.25 nm	288.9 ± 0.25 nm
FWHM	≤ 1.2 nm	≤ 1.2 nm
Low Channel [0-1.5 km]		
Telescope Diameter [cm]	2.5 cm	2.5 cm
FOV [mrad]	4.5	4.5
Detector (Hamamatsu)	7400P-03	7400P-03
Gates [km]	0.15	0.15
Neutral Density Transmittance [%]	5	10
Calculated Full Overlap Altitude [km]	0.105	0.105
Middle Channel [1.5 -5 km]		
Telescope Diameter [cm]	2.5 cm	2.5 cm
FOV [mrad]	4.5	4.5
Detector (Hamamatsu)	7400P-03	7400P-03
Gates [km]	0.415	0.415
Neutral Density Transmittance [%]	25	50
Calculated Full Overlap Altitude [km]	0.105	0.105
High Channel [3-12 km]		
Telescope Diameter [cm]	45 cm	45 cm
FOV [mrad]	1.0	1.0
Detector (Hamamatsu)	7400P-03	7400P-03
Gates [km]	3.015	3.015
Neutral Density Transmittance [%]	100	50
Calculated Full Overlap Altitude [km]	0.462	0.462
Data Acquisition System	Licel Transient Recorder (Model TR20-80) 300 Mhz Maximum Photon Counting Rate 16-bit, 50-ns range resolution	

Table 3: A list of the quantified uncertainties associated with the GSFC TROPOZ DIAL instrument during the test case on 25 October 2013

	Low Channel [0-1.5 km]	Middle Channel [1.5 -5 km]	High Channel [3-12 km]
Statistical Uncertainty	1-10%	1-16%	1-24%
Aerosol Correction	$< 12\%$	$< 2\%$	$< 2\%$
Rayleigh Correction	$< 1\%$	$< 1\%$	$< 1\%$
SO_2	-1%	-1%	-1%
NO_2	-0.5%	-0.5%	-0.5%
O_2 - Dimer	1.5%	1.5%	1.5%
Temperature Dependence of $\Delta\sigma_{O_3}$	3 %	3%	3%
Saturation Correction	10 %	5%	3%
Final Reported	16-19 %	10-18%	11-25%

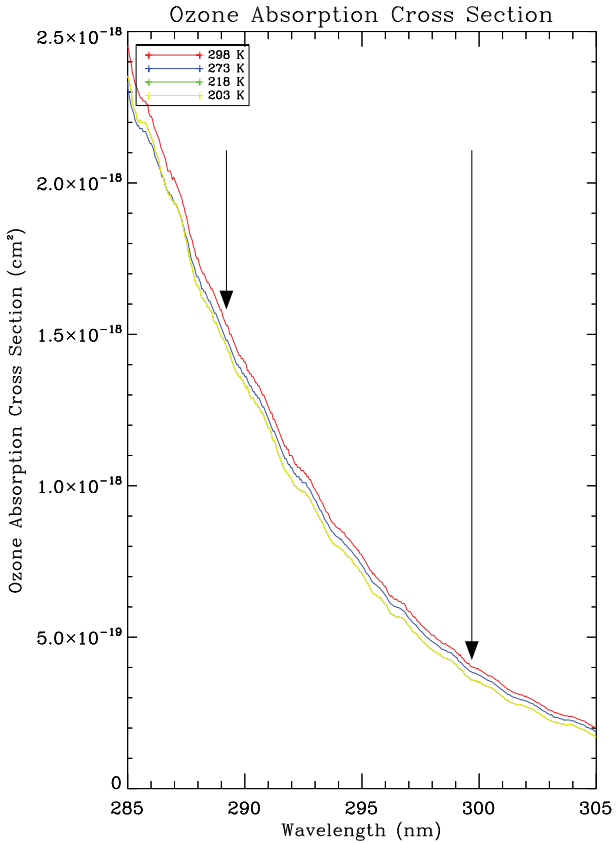

Fig. 1: The spectral dependence of the ozone absorption cross section in the UV. The more absorbing wavelength, at 288.9 nm, is called the "on" wavelength and the less absorbing wavelength, at 299.1 nm, is called the "off" wavelength. [Source: Malicet et al. (1995)]

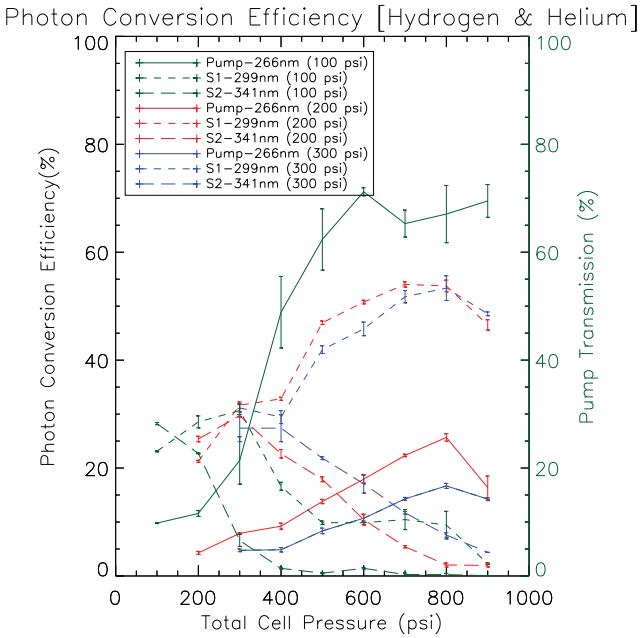

Fig. 2a: Photon conversion efficiency of hydrogen as function of total Raman cell pressure. The experiment was done with multiple partial pressures of hydrogen and helium, in which the the most efficient pressure combination of S1 was chosen for the GSFC TROPOZ DIAL. The pressures indicated in the legend are for the partial pressures of the Raman active gas. The uncertainty bars represent one standard deviation in the measurements.

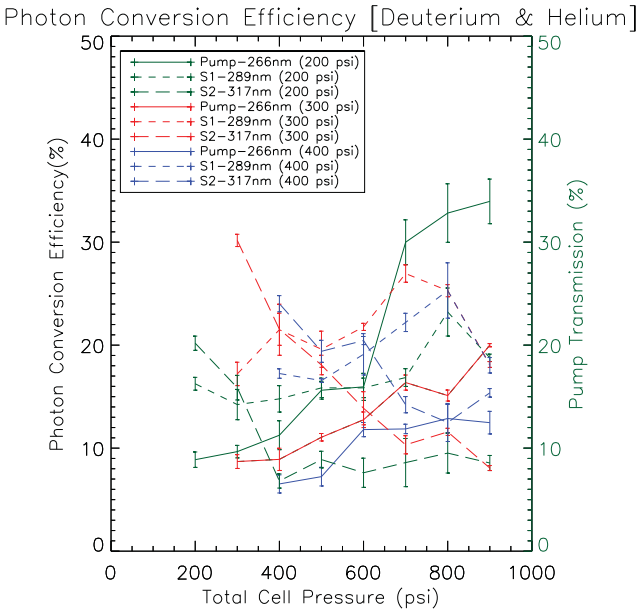

Fig. 2b: The experiment repeated for the multiple pressure combinations in the deuterium Raman cell.

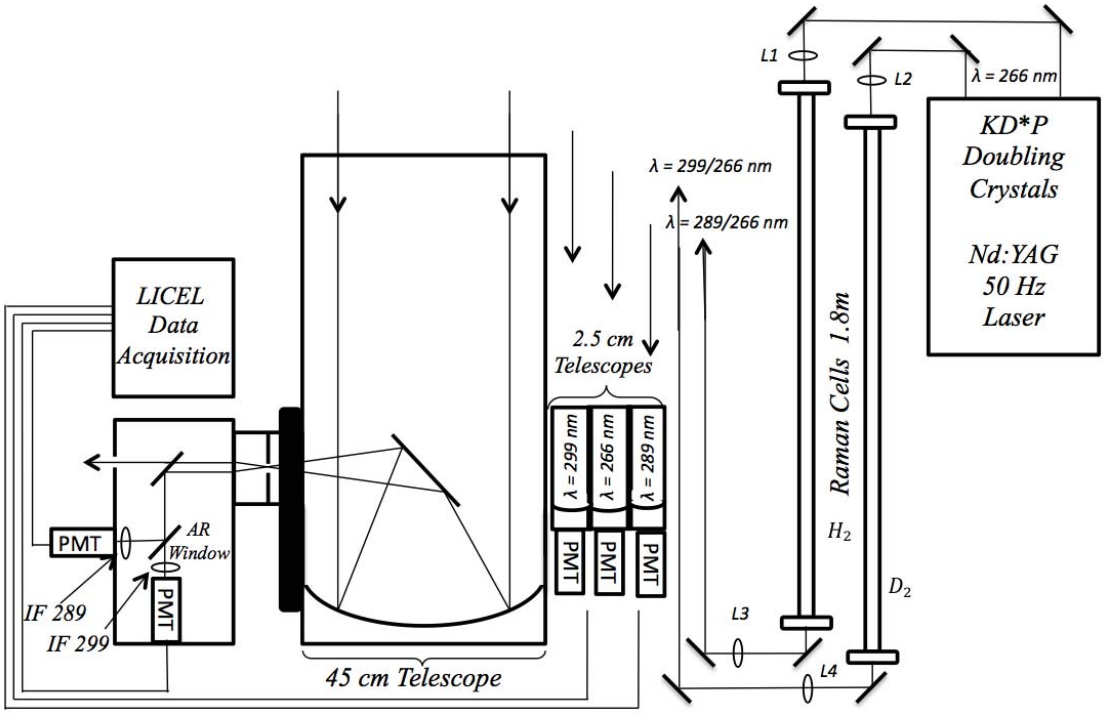

Fig. 3: The experimental schematic that includes the 50 hz Nd:YAG laser, steering optics, Raman cells, near field smaller telescopes, main telescope and detection packages.

Fig. 4: The 13 m trailer that houses the GSFC TROPOZ DIAL system. The hatch doors are open to transmit the DIAL wavelengths into the atmosphere.

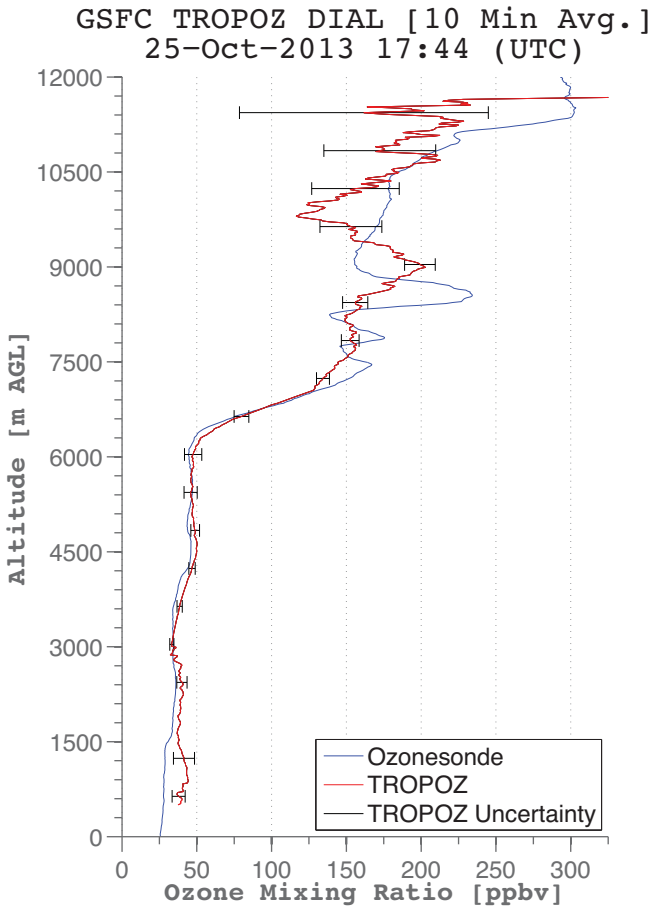

Fig. 5: The profile comparison for the GSFC TROPOZ DIAL retrieval (10 minute resolution) and the ozonesonde launch at 17:44 UTC on 25 October 2013 at Beltsville, MD. [Source: Howard University Beltsville Center for Climate Systems Observation]

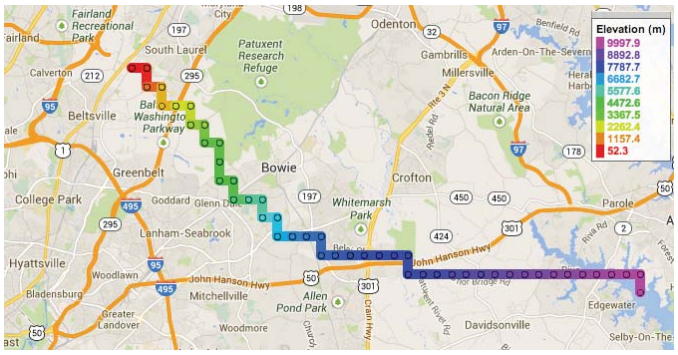

Fig. 6: Ozonesonde GPS coordinates during the ozonesonde flight. The color represents the altitude of the ozonesonde with the first red dot corresponding to Beltsville, MD. The TROPOZ site at GSFC is near the green section of the trajectory. When the sonde is above 7 km (light and dark blue) it is 16 km away from the lidar and at a altitude of 10 km (magenta) it is near 30 km away from the lidar. The altitude legend is on the right side of the figure. [Source: Howard University Beltsville Center for Climate Systems Observation; Map Source: Google Maps]

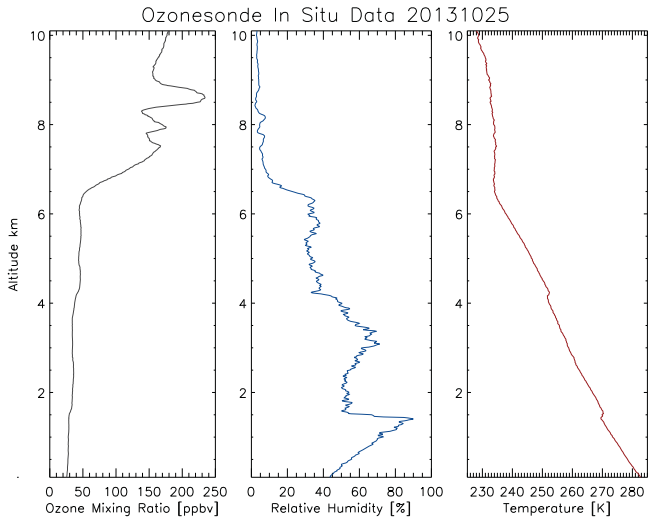

Fig. 7: The radiosonde and ECC in situ data for ozone mixing ratio, relative humidity, and temperature plotted for the test case on 25 October 2013. [Source: Howard University Beltsville Center for Climate Systems Observation]

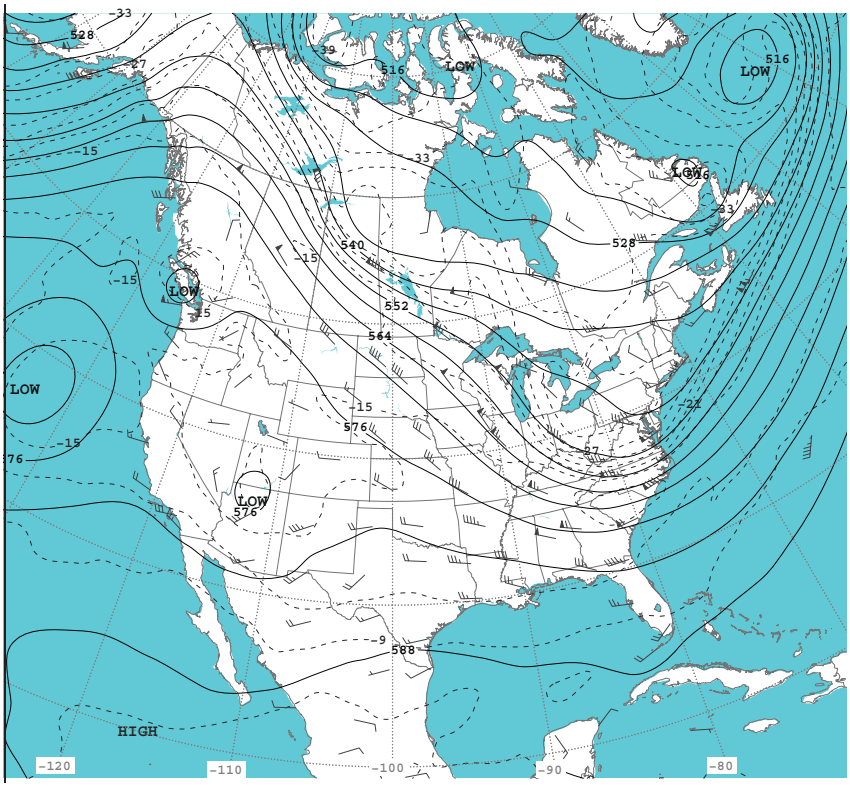

Fig. 8: A 500-millibar (mb) height contour national map for 11:00 UTC 25 October 2013, courtesy NOAA Daily Weather Map, for the meteorological events that surrounded the test case is shown. The figure shows height contours (solid lines), temperatures (dashed lines) and winds (arrows). The height contours show the height of the 500-mb pressure level in dekameters above sea level, the isotherms, or lines of constant temperature, are shown in degrees Celsius, and the arrows show the wind direction and speed at the 500-mb level. [Source: NOAA Daily Weather Map]

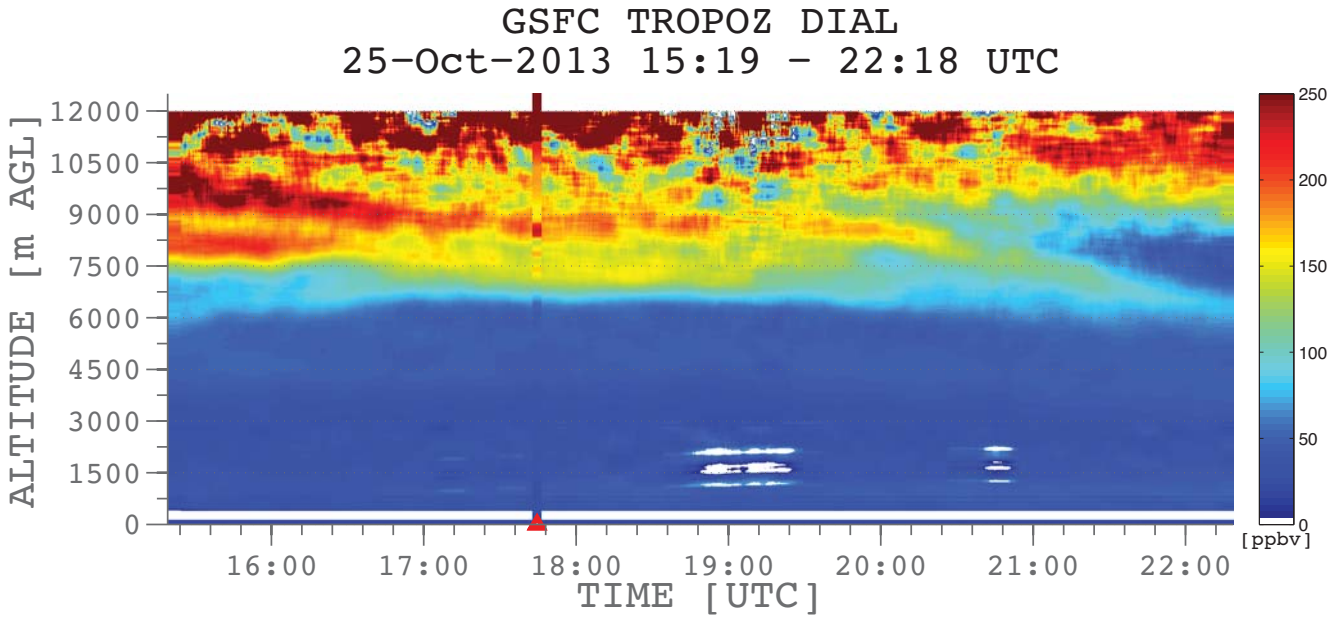

Fig. 9a: Time series plot of the ozone mixing ratio [ppbv] from the GSFC TROPOZ DIAL between 15:19-22:18 UTC (11:19 - 18:18 EST) at a 10 minute temporal resolution with the co-located ozonesonde launch corresponding to the red arrow point at 17:44 UTC. The surface ozone monitor mixing ratios (1 minute resolution) are plotted in the lowest bin of the figure.

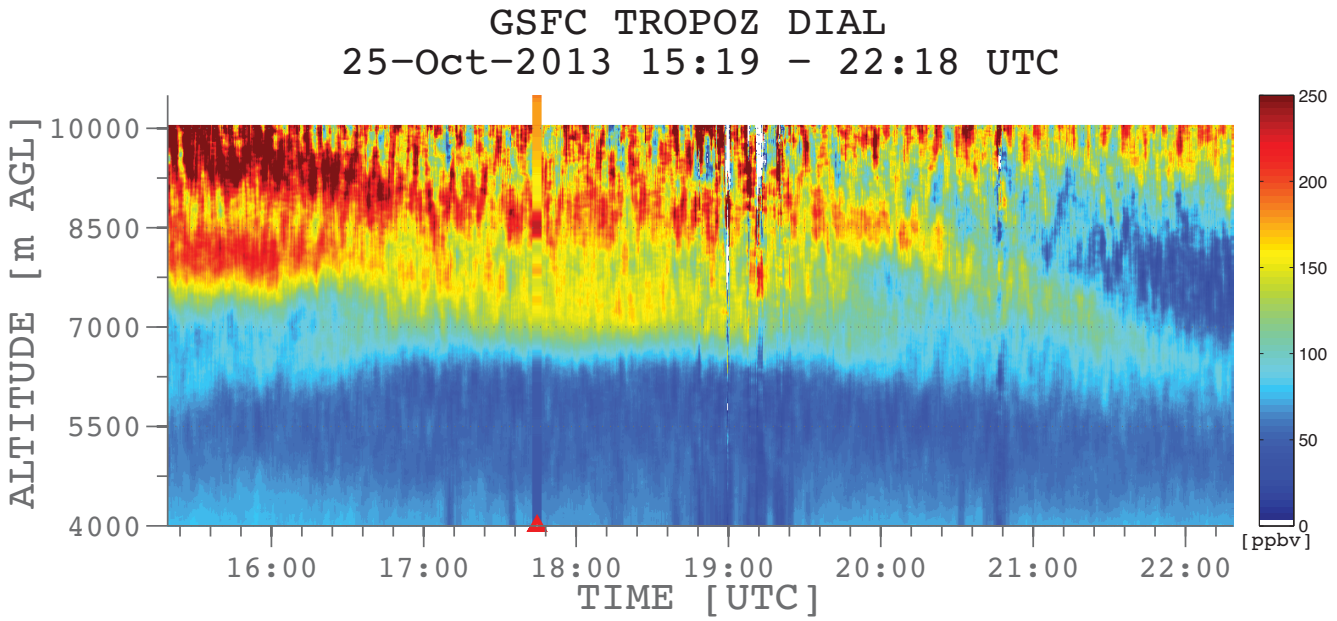

Fig. 9b: Time series plot of the ozone mixing ratio [ppbv] from the GSFC TROPOZ DIAL between 15:19-22:18 UTC (11:19 - 18:18 EST) at a 1 minute temporal resolution with the co-located ozonesonde launch corresponding to the red arrow point at 17:44 UTC. This plot focuses attention on the upper atmospheric conditions in order to represent the ability to monitor the changing dynamics of the ozone reservoir on a very short time scale.